Nanoscale

Quantum Capacitance-Limited MoS2 Biosensors Enable Remote Label-Free Enzyme Measurements

Journal:	*Nanoscale*
Manuscript ID	NR-ART-04-2019-003171.R2
Article Type:	Paper
Date Submitted by the Author:	02-Aug-2019

Complete List of Authors:	Le, Son; National Institute of Standards and Technology, Engineering Physics Division; University of Massachusetts Amherst, Department of Physics Guros, Nicholas; National Institute of Standards and Technology Bruce, Robert; National Institute of Standards and Technology Cardone, Antonio; National Institute of Standards and Technology Amin, Niranjana; National Institutes of Health Zhang, Siyuan; National Institute of Standards and Technology Klauda, Jeffery; University of Maryland Pant, Harish; National Institutes of Health Richter, Curt; National Institute of Standards and Technology, Semiconductor Electronics Division Balijepalli, Arvind; National Institute of Standards and Technology,

Quantum Capacitance-Limited MoS_2 Biosensors Enable Remote Label-Free Enzyme Measurements

Son T. Le[1,2], Nicholas B. Guros[3,4], Robert C. Bruce[1], Antonio Cardone[5,6], Niranjana D. Amin[7], Siyuan Zhang[1,2], Jeffery B. Klauda[4], Harish C. Pant[7], Curt A. Richter[1] and Arvind Balijepalli[3,*]

[1]Nanoscale Device Characterization Division, National Institute of Standards and Technology, Gaithersburg, MD 20899, USA ; [2]Theiss Research, La Jolla, CA 92037; [3]Microsystems and Nanotechnology Division, National Institute of Standards and Technology, Gaithersburg, MD 20899, USA;[4]Department of Chemical and Biomolecular Engineering, University of Maryland, College Park, MD 20742, USA; [5]Software and Systems Division, National Institute of Standards and Technology, Gaithersburg, MD 20899, USA; [6]University of Maryland Institute for Advanced Computer Studies, University of Maryland, College Park, MD 20742, USA; [7]National Institute of Neurological Disorders and Stroke, National Institutes of Health, Bethesda, MD 20892, USA

[*]e-mail: arvind.balijepalli@nist.gov

Abstract

We have demonstrated atomically thin, quantum capacitance-limited, field-effect transistors (FETs) that enable the detection of pH changes with 75-fold higher sensitivity (≈4.4 V/pH) over the Nernst value of 59 mV/pH at room temperature when used as a biosensor. The transistors, which are fabricated from monolayer films of MoS_2, use a room temperature ionic liquid (RTIL) in place of a conventional oxide gate dielectric and exhibit very low intrinsic noise resulting in a pH resolution of 92×10^{-6} at 10 Hz. This high device performance, which is a function of the structure of our device, is achieved by remotely connecting the gate to a pH sensing element allowing the FETs to be reused. Because pH measurements are fundamentally important in biotechnology, the increased resolution demonstrated here will benefit numerous applications ranging from pharmaceutical manufacturing to clinical diagnostics. As an example, we experimentally quantified the function of the kinase Cdk5, an enzyme implicated in Alzheimer's disease, at concentrations that are 5-fold lower than physiological values, and with sufficient time-resolution to allow the estimation of both steady-state and kinetic parameters in a single experiment. The high sensitivity, increased resolution, and fast turnaround time of the measurements will allow the development of early diagnostic tools and novel therapeutics to detect and treat neurological conditions years before currently possible.

Keywords: Field-effect transistor (FET), Room temperature ionic liquid (RTIL), MoS_2, Biosensor, Super-Nernstian, pH, Enzyme activity, Enzyme kinetics.

Introduction

Rapid and sensitive pH measurements based on field-effect transistors (FETs) are used in diverse applications that include determining the effects of ocean acidification on marine ecology,[1] biomanufacturing,[2] and low cost DNA sequencers.[3] However, drastic improvements in

sensitivity and the resolution of electronic pH transduction are needed to accelerate their widespread use in important biotechnology applications. One such example is the measurement of the function of enzymes, macromolecular catalysts that accelerate biochemical reactions and serve an integral role in ensuring normal cellular function,[4] where small changes in the solution pH act as a reporter of their function.[5,6] Disruptions in normal enzyme function are known to give rise to debilitating neurological conditions including Alzheimer's and Parkinsons's disease,[7] several cancers,[8] and even chronic neuropathic pain.[9] As part of normal cellular function, enzymes catalyze the phosphorylation of substrate proteins by the hydrolysis of adenosine triphosphate (ATP) and the transfer of a single phosphate group. This results in the release of one or more protons into solution, and thereby a small change in the pH. The change in pH typically varies by less than 0.005 units[10,11] under physiological conditions (i.e., for normal living organisms) or an order than magnitude lower than the resolution demonstrated with state-of-the-art ion-sensitive field-effect transistors (ISFETs).[3,12]

Several techniques have been developed over the past century for more accurate measurements of solution pH. The Harned cell is the primary pH measurement standard,[13] but it requires an elaborate setup and long equilibration times making it unusable in the measurement of small and fast pH changes. As a result, pH measurements used in biotechnology applications rely extensively on electrode measurements or spectrophotometric techniques. These approaches lack adequate sensitivity and resolution for accurate measurements of enzyme-mediated pH changes.[14,15] Over the past several years, there have been numerous developments in pH sensing technology using solid-state devices that are potentially suitable for biological applications.[3,12,16,17] Improved sensitivity and dynamic measurements have been demonstrated with ISFETs[3] and more recently dual-gate silicon FETs.[16] In the latter case, pH sensitivity was

shown to be approximately two-fold higher than the Nernst potential of ≈59 mV/pH at room temperature.[17] Notably, the resolution of ISFETs has been reliably demonstrated to be 0.05 pH units.[3,12] The resolution for these devices could be lower if the device parameters are optimized[18] or if the measurements are performed under a very narrow bandwidth.[19] However, resolution that is adequate for enzyme measurements under physiological conditions are yet to be experimentally realized with silicon FETs. These limitations have required FET-based enzyme catalyzed phosphorylation assays to be performed at concentrations that are about two orders of magnitude higher than physiological values, precluding their use in diagnostic and therapeutic development applications.[6,20,21]

Here, we show that FETs with an atomically thin semiconducting channel and gated with an ionic liquid (2D-ILFET) allow label-free measurements of enzyme activity and kinetics at or below physiological concentrations. The measurements were performed by using a pH sensing element that is connected electrically to the 2D-ILFET (Figure 1a). This configuration allowed measurements with both a high intrinsic gain[16] (i.e., sensitivity) and signal-to-noise ratio (SNR) that exceeded comparable silicon devices by more than an two orders of magnitude.[22] We show that the newly-developed 2D-ILFET measurements are a quantitative first step to enabling their use in drug discovery and diagnostic applications. The ability to perform measurements within current testing frameworks and without resorting to surface modification[5,20,23] or hazardous radioactive labeling will enable rapid adoption of the method. Furthermore, the higher sensitivity of the technique will allow its use in applications beyond enzymatic measurements, for example in critically needed early detection of neurodegenerative conditions,[24] and more broadly to the measurements of biomolecular interactions that are important in many applications in biophysics and biotechnology.[3,25-27]

In order to optimize the use of ionic liquid-gated 2D-ILFETs in enzyme activity measurements, we first characterized their electrical performance, followed by sensitive pH measurements to validate the approach. The optimized configuration was then used to measure the activity and kinetics of the proline directed kinase Cdk5,[28] an enzyme strongly implicated in several neurodegenerative conditions.

Experimental

Device Fabrication and Characterization: High-performance FETs were fabricated using a technique we recently developed.[29] Briefly, large area and high quality monolayer MoS_2 flakes were exfoliated from bulk crystal using a gold-mediated exfoliation method[30] on to oxidized, heavily doped silicon substrates that also served as a global back-gate. The thickness of the films was verified using photoluminescence and Raman spectroscopy as shown in Figure S8. The SiO_2 substrates with a thickness of 300 nm and 70 nm were used to study the device performance scaling. After the monolayer MoS_2 flakes were located and inspected using an optical microscope, optical photolithography was used to pattern the source, drain, and gate electrodes followed by electron beam evaporation of metal Ti/Au (2 nm/100 nm) and lift-off in acetone. A second photolithography step was used to define the active channel area, followed by reactive ion etching to remove excess MoS_2 outside the channel area. After a final resist cleaning, a small droplet of the DEME-TFSI IL† (727679; Sigma Aldrich, St. Louis, MO) was carefully applied onto each device using a micromanipulator and an optical microscope. The droplet was sized to cover the MoS_2 monolayer and the gate electrodes,[31,32] as seen in the optical image of the final device in Figure 1b. It is important to note that for good ionic liquid-gate coupling with the device's channel, the area of the gate electrodes that is in contact with the ionic liquid was designed to be much larger than the combined area of the source, drain contacts, and MoS_2

channel that are in contact with the ionic liquid. Gate leakage was verified by measuring the current across the ionic liquid upon application of a potential across two patterned gate electrodes. The measurement scheme for electrical characterization is shown Figure 1a.

Effect of contact resistance on the device performance: For the ionic liquid gated MoS_2 FET biosensors presented here, the effects of poor contacts should be minimal since the devices are always operated in the inversion regime to achieve high gain. The high channel carrier density in this regime greatly diminishes the effect to the Schottky barrier at the contacts allowing carriers to be injected into the channel with little difficulty. However, future work using these devices will build upon the contact engineering that we have developed[29] to further improve sensitivity and the signal-to-noise ratio (SNR).

Effects of ionic liquid hysteresis: Room temperature ionic liquids can introduce considerable hysteresis during bidirectional voltage sweeps of the biosensor. This effect is insignificant when measuring very small pH changes, for example during enzyme measurements, and is not a very large source of error. However, hysteresis can be more pronounced for large pH measurements. To mitigate this effect, we always operate the device by sweeping V_{BG} in one direction when the liquid gate is connected to the measured solution. This method of operation minimizes hysteresis and allows reproducible measurements over a wide pH range.

Quantum Capacitance Model: For a monolayer MoS_2 FET under positive ionic liquid-gate bias, the relationship between gate voltage, V_{LG}, and the channel charge carrier density, n_{ch}, is given by,[33,34]

$$V_{LG} - V_{t,LG} - V_{FB} = \frac{E_g}{2q} - \frac{k_B T}{q} ln\left[exp\left(\frac{n_{ch}}{g_{2D} k_B T}\right) - 1\right] + \frac{q n_{ch}}{C_{LG}} \qquad (1)$$

where $V_{t,LG}$ is device threshold voltage, V_{FB} is the flat band voltage, Eg is the material band gap, q is elementary charge, k_B is Boltzmann's constant, T is the temperature in Kelvin, g_{2D} is the band edge density of states, and C_{LG} is the liquid-gate capacitance. For a fixed V_{LG}, we calculated $V_{t,LG}$ as a function of channel carrier density,

$$V_{t,LG} = V_{LG} - V_{FB} - \left\{\frac{E_g}{2q} - \frac{k_B T}{q} ln\left[exp\left(\frac{n_{ch}}{g_{2D} k_B T}\right) - 1\right] + \frac{q n_{ch}}{C_{LG}}\right\} \quad (2)$$

The channel quantum capacitance (C_Q) is dependent on the density of charge carriers within the channel and is given by,[33]

$$C_Q \approx q^2 g_{2D}\left[1 + \frac{\exp\left(\frac{E_g}{2k_B T}\right)}{2cosh\left(\frac{qV_{ch}}{k_B T}\right)}\right]^{-1}, \quad (3)$$

where

$$V_{ch} = \frac{E_g}{2q} - \frac{k_B T}{q} ln\left[exp\left(\frac{n_{ch}}{g_{2D} k_B T}\right) - 1\right] \quad (4)$$

Using Equations 1—4 we calculated $V_{t,LG}$ and C_Q as a function of n_{ch}. Since C_{TG} and C_Q are in series as seen from Figure 1e, we calculate $C_{TG}(C_Q) = C_{LG} \times C_Q/(C_{LG}+C_Q)$, where C_{LG} is the ionic liquid-gate capacitance. Similarly, the back-gate capacitance, $C_{BG} = C_{ox} \times C_Q/(C_{ox}+C_Q)$, where C_{ox} is the back-gate oxide capacitance. Moreover, since $C_Q >> C_{ox}$, $C_{BG} \approx C_{ox}$=constant. Under these limits, the expression for α is given by,

$$\alpha = \frac{C_{TG}}{C_{BG}} \approx \frac{C_{LG}\, C_Q}{C_{ox}(C_{LG} + C_Q)} \qquad (5)$$

and is limited by C_Q. At large values of n_{ch}, C_Q approaches its theoretical limit, $C_{Q,max}$, and α is constant. As n_{ch} decreases, C_Q decreases exponentially from $C_{Q,max}$ and we observe a corresponding reduction in α. The results from the model were compared with experimentally measured values of α, which were extracted by numerically estimating the derivative dV_{BG} $/dV_{t,LG}$ (Figure 1d and Figure S2; *Supplementary Information*).

Time-Series Field-Effect Transistor Measurements and PID Control: Time-series measurements were performed following the schematic in Figure 2a. The signal on the ionic liquid-gate (V_{LG}) was switched between an arbitrary function generator (HF2LI; Zurich Instruments, Zurich, Switzerland) or a pH microelectrode (MI-4156; Microelectrodes, Bedford, NH). An offset voltage, V_o (GS200; Yokogawa Corporation, Tokyo, Japan), was then added to V_{LG} using a summing amplifier (SR560; Stanford Research Systems Inc., Sunnyvale, CA). The FET was operated in a constant current mode using a PID controller that varied V_{BG} in response to changes in I_D. The channel current was first amplified using a current preamplifier (DLPCA-200; FEMTO, Berlin, Germany) with a transimpedance gain of 10^6 V/A. The amplified voltage was input to a digital PID controller (HF2LI; Zurich Instruments, Zurich, Switzerland), filtered using a 4-pole Bessel low pass filter (LPF) with a bandwidth of 5 kHz and then sampled at 25 kHz using a 14-bit analog to digital converter. The PID controller varied V_{BG} in response to changes in I_D with a bandwidth of 1 kHz (K_P=496.1, K_I=9.242×10^3 s^{-1} and K_D=8.02 μs). The PID output was used to drive the back-gate voltage (V_{BG}) between -10 V to +10V.

Ionic Liquid-Gate C-V Measurements: In order to verify the capacitance of the ionic liquid (C_{LG}), we utilized a LCR meter (E4980A; Agilent, Santa Clara, CA) to make 2-probe, AC capacitance measurements across the ionic liquid, measuring across a frequency range of 20 Hz to 2 MHz. Figure S3 (see *Methods*) shows representative results of these capacitive measurements, highlighting that at low frequency (where our devices typically operate for sensing) the capacitance constant and approximately 1 nF. As seen in the inset, we observe a negligible bias dependence of the capacitance at all measured frequencies. The capacitance exhibits a less than 1% change over a ± 0.5 V range at the lowest frequency (20 Hz). Due to the design of our devices, we do not have a constrained contact area of the ionic liquid on electrodes, therefore we utilized optical estimates of ≈100 μm × 100 μm as the area of metal plates that are in contact with the ionic liquid used in the capacitance measurement. This allowed us to estimate the specific gate capacitance to the liquid-gate to be ≈10.7 μF/cm^2 at low frequency range (20 Hz to 2 kHz), in good agreement with values published in the literature.[35]

Resolution of pH Measurements: The pH resolution was established by using two approaches: i) from a measurement of the power spectral density (PSD) of noise in V_{BG} and ii) from the uncertainty in time-series measurements in constant current mode.

i) *Power Spectral Density Method:* The PSD of V_{BG} was measured as shown in Figure S4. The broadband root mean squared (RMS) noise under PID control was then obtained using the expression $\delta V_{BG} = \sqrt{\int_{BW} S_{V_{BG}} df}$, where $S_{V_{BG}}$ is the noise density, df is the frequency bin and BW is the low-pass filter bandwidth. Using common conventions in signal processing and in the literature,[19,36] we defined minimum detectable value of V_{BG} to be that at a SNR of 3 (or ≈10 dB). This allowed the determination of the pH resolution, represented throughout the

manuscript by δpH_{PSD}, using the expression, $\delta pH_{PSD}=3\times\delta V_{BG}/(\alpha V_{Nernst})$, where V_{Nernst}=59.5 mV/pH is the Nernst voltage at room temperature.

ii) *Time-Series Uncertainty:* The pH resolution measured from the uncertainty of time-series measurements is represented by δpH. The uncertainty in V_{BG} in constant current mode was obtained by first computing the histogram of the time-series at varying values of pH. Each resulting histogram was fit to a normal distribution with mean, μ_{VBG} and standard deviation, σ_{VBG}. The uncertainty in V_{BG} is reported with an expanded uncertainty, k=2. This allows the pH resolution to be computed using the expression $\delta pH=k\sigma_{VBG}/(\alpha V_{Nernst})$.

Kinase Measurement Reagents: Static activity measurements of Cdk5/p25 phosphorylation of histone H1 were performed by suspending 100 ng of the enzyme (C0745; Sigma Aldrich, MO) in 50 μL of 1× kinase buffer to obtain a final concentration of 18.5 nM. The Cdk5/p25 concentration was reduced five-fold for dynamic measurements to obtain a final concentration of 3.7 nM. A stock solution of 5× kinase buffer was prepared by suspending 25 mM β-glycerol (G9422; Sigma Aldrich, MO), 50 mM $MgCl_2$ (5980; Millipore, MA), 5 mM EGTA (E0396; Sigma Aldrich, MO), 2.4 mM EDTA (1002264786; Sigma Aldrich, MO), 1.25 mM MOPS (M1254; Sigma Aldrich, MO) in deionized water (DIW) and diluting further to form 1× kinase buffer. Solutions of the substrate protein were prepared by adding 2 mg/mL of histone H1 (10223549001; Sigma Aldrich, MO) to the assay to obtain the final concentrations as described in the main text. The phosphorylation reaction was triggered with a cocktail of DTT and ATP. The final concentration of the ATP and DTT solution was adjusted to 250 μM and 5 mM in DIW respectively.

Cdk5 γ-^{32}P-ATP Measurements: Cdk5/p25 (C0745; Sigma Aldrich, MO) kinase activity was measured as described in the manufacurer's protocol with some modifications. The kinase

reaction was initiated by adding γ-^{32}P-ATP (final concentration of 50 μM) to a preincubated substrate buffer cocktail and incubated at 30 ^{o}C for 1 hour. The reaction was terminated by spotting 20 μl of the reaction mixture on a P81 phosphocellulose pad. Dried pads were washed 3 times in 75 mM phosphoric acid, followed by rinsing with 95% ethanol. The radioactivity of the spotted pads was measured in a liquid scintillation counter. Appropriate controls, without added phosphoryl acceptor substrates, were also run and the values were subtracted from the total counts obtained in the presence of substrate protein.

Results and Discussion

Ionic Liquid-Gate 2D FET Performance. Initial characterization of 2D-ILFETs fabricated with monolayer MoS_2[37] was performed with the set up in Figure 1a and using a representative device seen in Figure 1b (see *Methods* for fabrication details) where the sensing signal was connected to the top ionic liquid gate, while the silicon substrate was used as the measurement gate. The devices described in this work are fundamentally different from dual-gate silicon FETs[16,38] in that the asymmetric, capacitively coupled, gates in the 2D-ILFET control the same atomically thin semiconducting channel giving rise to a large intrinsic gain in conjunction with ultralow noise performance. Furthermore, the measurement setup allowed the 2D-ILFET performance to approach the intrinsic quantum capacitance limit of the channel material.

The transfer characteristics of the device were measured by recording the drain current (I_D) as a function of the liquid-gate potential (V_{LG}) with the drain voltage (V_D) was held constant. The measurements were repeated for different back-gate voltages (V_{BG}) to determine the signal amplification (α) due to the asymmetric capacitance of the ionic and back gates (Figure 1c). The

devices exhibited a dynamic range of ≈5 orders of magnitude in I_D and a subthreshold slope between 69 mV/dec and 145 mV/dec at ≈300 K.

For each curve in Figure 1c, the liquid-gate threshold voltage ($V_{t,LG}$) was determined from a linear extrapolation of the peak transconductance to the *x*-axis.[39] The value of $\alpha = dV_{BG}/dV_{t,LG}$ for representative devices was then determined numerically from the data in Figure 1d (d=300 nm) and Figure S2 (d=70 nm; see *Supplementary Information*), where d is the thickness of the back-gate dielectric. From Figure 1d we can clearly discern two distinct regimes for V_{BG} as a function of $V_{t,LG}$. At large and positive V_{BG} (Figure 1d; *pink*), where the device was in the limit of large 2D channel carrier density (n_{ch}), α was constant and found to be 156±3 (d=300 nm) and 41±4 (d=70 nm). On the other hand, at negative V_{BG} and low n_{ch} (Figure 1d; *blue*), α decreased exponentially. Both regimes of operation are explained by the quantum capacitance model discussed next. The error bars report the standard error defined as the standard deviation of the population mean.

Quantum Capacitance-Limited Performance. For devices with two gates, α can also be determined from the ratio of the top (C_{TG}) and bottom gate (C_{BG}) interface capacitances, i.e., $\alpha \approx C_{TG}/C_{BG}$ (see *Supplementary Information* for a detailed derivation).[16,31,40] For dual-gate FETs where the individual gate oxide capacitances are considerably lower than those associated with the channel, α is constant and can be calculated directly from the properties of the gate dielectric.[35] However, due to the large capacitances associated with ionic liquids, for the devices reported here C_{TG} is limited by the intrinsic quantum capacitance (C_Q) of the 2D semiconducting channel. Importantly, C_Q approaches its theoretical limit, $C_{Q,max}$ when n_{ch} is large.[33] Under these conditions α is constant. On the other hand, when n_{ch} is reduced, C_Q and therefore α decrease

exponentially (see *Methods* for a detailed explanation). This transition between the linear and exponential regimes can be observed in terms of the gate voltage in Figure 1d and α in Figure 1f.

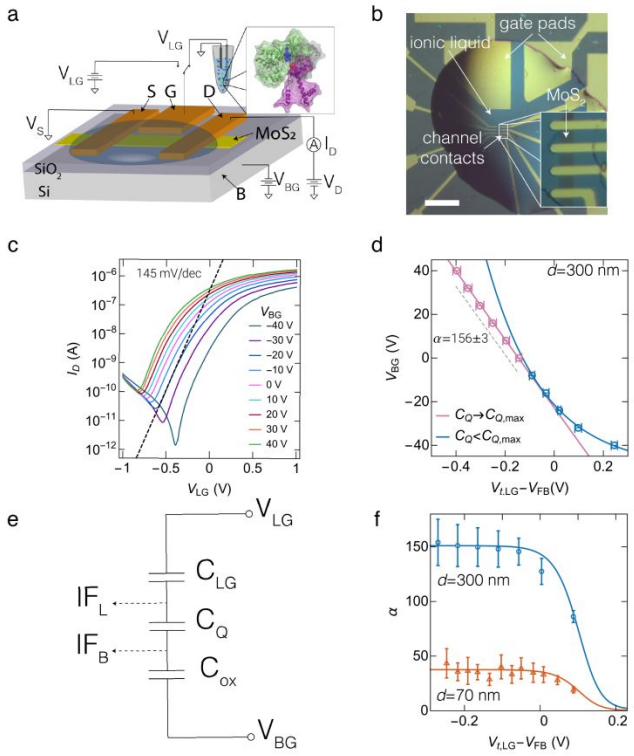

Figure 1: Electrical characterization of ionic liquid-gate field-effect transistors (FETs). Error bars report standard errors defined as the standard deviation of the population mean. (a) Device schematic of an ionic liquid-gated FET for biosensing. A semiconducting channel formed between the source (*S*) and drain (*D*) terminals is controlled electrostatically by a voltage applied to the silicon substrate (*B*) or the ionic liquid top-gate (*G*). A voltage applied to the ionic liquid-gate (V_{LG}) can be switched between a voltage source for characterization or a biosensing element. The biosensing element used in this work is a glass pH microelectrode connected remotely to the top-gate contact. (b) An array of ionic liquid dual-gate FETs fabricated using a 2D MoS_2 film on a 300 nm SiO_2 substrate. The scale bar represents 100 μm. (c) Transfer characteristics show the drain current (I_D) as a function of V_{LG} and varying back-gate voltage (V_{BG}). (d) The change in V_{BG} as a function of liquid-gate threshold voltage ($V_{t,LG}$). A flat band voltage (V_{FB}) of -0.82 V was subtracted from $V_{t,LG}$ to enable comparison with theory. (e) The dual-gated FET was modeled with three capacitors in series. The quantum capacitance (C_Q) of the 2D channel controls the capacitive coupling between the back (IF_B) and liquid (IF_L) gate interfaces. (f) A plot of α as a function of $V_{t,LG}$ for two devices with back-gate oxide thickness of 300 nm (○) and 70 nm (□). The solid line shows the theoretical model for quantum capacitance limited device performance. V_{FB} =–0.82 V (d=300 nm) and V_{FB} =+0.12 V (d=70 nm) were subtracted from $V_{t,LG}$ to allow direct comparison between devices.

We see quantitative agreement between the model and measurements for two representative device structures shown in Figure 1f. In both cases, we assumed C_{ox}=0.0115 μF/cm^2 (d=300 nm)

and 0.049 μF/cm^2 (d=70 nm), and C_{LG}=10.7 μF/cm^2 based on our own measurements (Figure S3; see *Supplementary Information*) and literature values.[35] $C_{Q,max}$ was directly calculated from Equation 5 (see *Methods*) to be 2.16 μF/cm^2, and was in excellent agreement with the value of 2.2±0.05 μF/cm^2 extracted from a non-linear regression of the model to the data in Figure 1f. The only other free parameter in the model was the flat band voltage (V_{FB}), which depends in part on the fabrication process.[41] The extracted value of $C_{Q,max}$ was within ≈45 % of the maximum theoretical value for monolayer MoS_2, and more than two times higher than previous measurements.[35,42] This in turn allowed the devices to operate with high sensitivity when used for enzyme measurements. Furthermore, the ability to tune α with only the gate voltage is advantageous in biosensing applications to allow sensitivity to be offset for higher dynamic range.

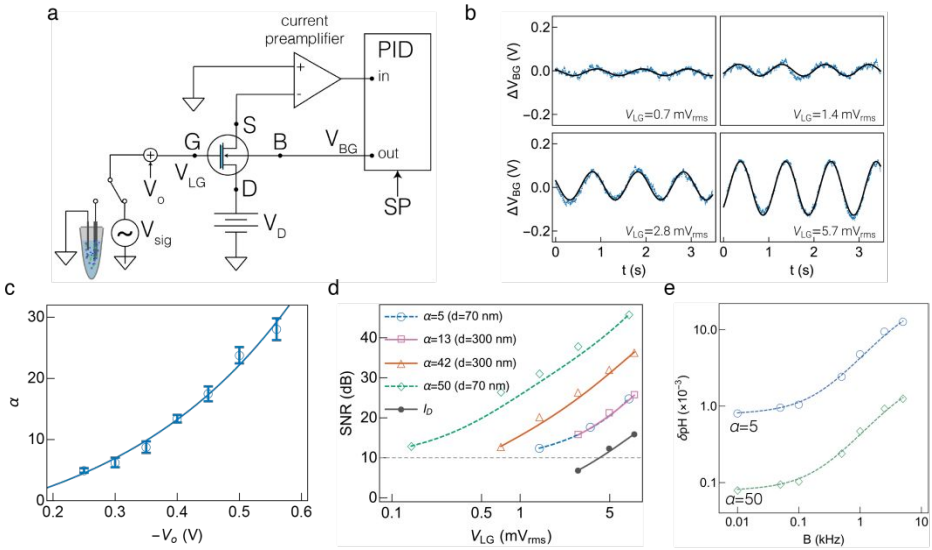

Figure 2: Constant current mode electrical characterization of dual-gated ionic liquid-gated field-effect transistors (FET). (a) The FETs were operated in a constant current mode using a proportional-integral-derivative (PID) controller. I_D was held constant by continually adjusting V_{BG} in response to small changes to V_{LG}. (b) The response of V_{BG}, under PID control, as a function of time is shown upon application of a 1 Hz AC sine wave signal with varying amplitude to the ionic liquid-gate. Data are shown for a back-gate oxide thickness, d=300 nm. (c) The amplification at the back-gate (α) increased with the applied liquid-gate offset voltage, V_o, allowing the device gain to be smoothly tunable. The error bars report the standard error defined as the standard deviation of the population mean. (d) The signal-to-noise ratio (SNR) was extracted with a bandwidth of 5 kHz as a function of AC signal amplitude for devices operated under PID control and in open loop (●). For devices fabricated with either a 300 nm (α =13; ⊟ and

α=42; ▲) or 70 nm (α =5; ○ and α =50; ◇) SiO_2 back-gate dielectric, the SNR under PID control was higher than under open loop operation. (e) The pH resolution (δpH) as a function of the measurement bandwidth and α for devices with a 70 nm (α =5; ○ and α =50; ◇) SiO_2 back-gate dielectric.

Constant Current Operation for Biosensing. The preceding results were used to maximize α when operating the ionic liquid FETs in a constant current mode using a proportional-integral-derivative (PID) controller as shown in Figure 2a. The PID controller varied V_{BG} in response to V_{LG} to maintain a root mean squared (RMS) channel current of 100 nA. PID performance was then compared with open loop operation where I_D was recorded in response to changes in V_{LG}. The signal connected to the ionic liquid-gate was setup to allow switching between an arbitrary waveform generator to calibrate sensor performance or a biosensing element. In both cases, a fixed DC offset voltage (V_o) was added to V_{LG} to set the value of α (see *Methods*).

Device Sensitivity. Device calibration was performed with a 1 Hz sine wave applied to the ionic liquid-gate. Figure 2b shows the change in V_{BG} (d= 300 nm) under PID control with V_o=–0.56 V for sine wave amplitudes of V_{LG} ranging from 0.7 to 5.7 mV_{rms}, which resulted in α=28. Tuning V_o allowed sensitivity to be smoothly offset for dynamic range with the highest α realized when operating near the linear regime determined from Figure 1d. Using this approach, we tuned α smoothly from 5±0.4 to 28±1.8 (Figure 2c) when d=300 nm or from 5±0.5 to 50±1.5 when d=70 nm. Moreover, the measured values of α were consistent with those in Figure 1f, and more than an order of magnitude higher than dual-gate silicon FET measurements.[16]

Signal-to-Noise Ratio and Resolution. The signal-to-noise ratio (SNR) is a true measure of sensor performance. To determine if the higher sensitivity of our FETs, relative to dual-gate silicon devices,[16] translated to an improved resolution, we measured the noise in V_{BG} and I_D of the 2D-ILFET devices as shown in Figure S4. These measurements were then used to determine the SNR of the FET in PID and open loop modes. Figure S4 shows a representative power

spectral density (PSD) of the back-gate voltage (*top*) under PID control (d=300 nm) and channel current (*bottom*) during open loop operation. The broadband noise under PID control was obtained using the expression $\delta V_{BG} = \sqrt{\int_{BW} S_{V_{BG}} df}$, from DC to the low pass filter bandwidth of 5 kHz and found to be 5.0 mV_{rms} (d=300 nm; Figure S4 *top*) and 0.45 mV_{rms} (d=70 nm; Figure S4 *middle*) for the measured devices, decreasing as expected with the back-gate oxide thickness. Furthermore, δV_{BG} was found to be invariant with V_o, and thereby α, over the measured range of biasing conditions. The channel current noise in the open loop case, $\delta I_D = \sqrt{\int_{BW} S_{I_D} df}$ was 700 pA_{rms} (Figure S4 *bottom*). The SNR was determined using the expressions $20\ log_{10}(V_{BG}/\delta V_{BG})$ under PID control and $20\ log_{10}(I_d/\delta I_d)$ in open loop mode and shown in Figure 2d as a function of V_{LG}. For a bandwidth of 5 kHz, SNR was found to increase ≈3-fold (α=13, d=300 nm) to ≈30-fold (α=50, d=70 nm) under PID control when compared to open loop operation.

The device structures described here are fundamentally different from silicon-based dual-gated FETs described in previous studies.[16,38] In those devices, it was interpreted that two channels were formed and controlled independently by the top and bottom gates. In constant current mode, when the device was operated in the inversion-inversion regime, changes in the gate potential at one interface that drive the corresponding channel into strong inversion (increasing channel current), cause the other channel to be placed into weak inversion (with increasing channel noise). Regardless of the polarity of the applied potential at the sensing gate, the overall channel current noise is dominated by the channel in weak inversion. Channel noise could further limit SNR when the devices are operated in the inversion-depletion regime, for example as demonstrated with ultra-thin body double-gated silicon FETs.[16] In this case, the noise is dominated by the depleted channel and should result in lower performance compared to the

inversion-inversion regime. Furthermore, this effect becomes more pronounced with increasing gain. As a result, extensive work with such devices has shown no measurable improvement in SNR of silicon devices despite large improvements in the sensitivity.[38] In contrast, ultra-thin channels formed with 2D materials have a single conducting channel controlled by both the top ionic liquid-gate and bottom SiO_2 back-gate. Because the channel can always be placed in the inversion regime, the relative noise is low over a wide range of biasing conditions leading to improved SNR with these devices.

The pH resolution, δpH_{PSD} (as defined in the *Methods*) was obtained from the PSD of V_{BG} at a temperature of 300 K. At a bandwidth of 5 kHz, the minimum detectable V_{BG} was 3.8 mV (α=50, d=70 nm) resulting in a δpH_{PSD} =0.0013 pH units for these conditions. Since the measurements of the kinetics of biomolecules are relatively slow, resolution can be further improved at lower bandwidth. This is possible because applying a low-pass filter to the data reduces noise at frequencies outside the desired signal bandwidth, thereby increasing the SNR.[43] When the signal was measured with a bandwidth of 10 Hz (Figure 2e; α=50, d=70 nm), we extracted a δpH_{PSD} =92×10^{-6} pH units, representing a greater than 10-fold improvement over state-of-the art ISFET measurements.[1,12,18,19] Importantly, in contrast to measurements made with dual-gate Si FETs, the resolution improved with increasing α as discussed above.

Sensitive pH Measurements. The ionic liquid-gate FETs were used to remotely measure the pH of buffered solution with high sensitivity. In this measurement, I_D was measured as a function of V_{BG} with a pH sensor measuring standard buffer solutions was connected to the liquid-gate as seen in Figure 3a. The change in the back-gate threshold voltage, $V_{t,BG}$ for each measured pH from 4 to 10 is apparent from the data in Figure 3b and was found to be linear (Figure 3c) as a

function of pH. The measurement sensitivity was ≈4.4 V/pH or 75× higher than the Nernst limit of 59 mV/pH at room temperature[17] (Figure 3c) and is a function of the device's intrinsic α.

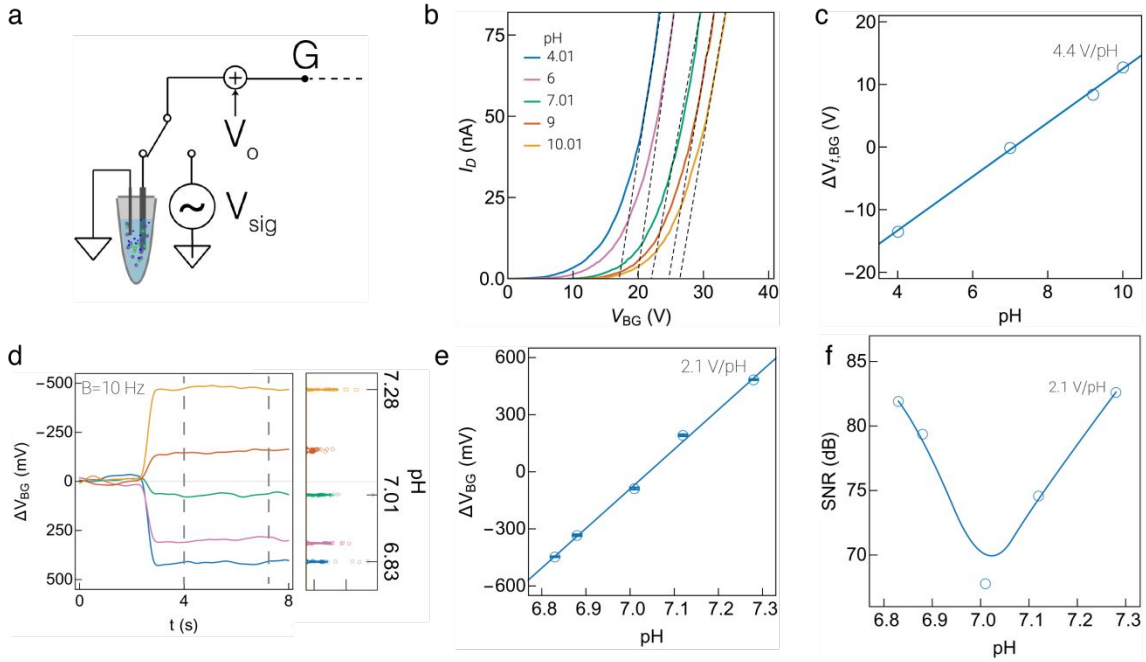

Figure 3: Ionic liquid-gate field-effect transistor (FET) calibration with buffered pH solutions. (a) Measurements of pH were performed by connecting the ionic liquid-gate (G) to a pH sensing element. The dashed line shows the connection to the FET. (b) The change in the back-gate threshold voltage ($\Delta V_{t,BG}$) as a function of the solution pH showed a linear response over the measured range. When using a 300 nm SiO_2 back-gate, the pH sensitivity was found to be 4.4 V/pH (○). (c) pH sensitivity of buffered electrolyte solutions was extracted from the shift in $\Delta V_{t,BG}$. Measurements were performed over a wide range of solution pH from 4.01 to 10.01. (d) Time-series measurements of V_{BG} response to buffered pH solutions were measured in constant current mode with a bandwidth, B=10 Hz, and when the device gain, α=33 (⊖). The panel on the right shows the histogram of V_{BG} for data points between the gray dashed lines. (e) The back-gate voltage (V_{BG}) response to varying pH buffer solutions, resulted in a sensitivity of 2.1 V/pH. The error bars represent the uncertainty in the measurement, obtained from the widths of the histogram in panel d. (d) The measurement signal to noise ratio (SNR) was measured at a bandwidth of 10 Hz and found to average 75 dB (≈5600). SNR was lowest in the vicinity of neutral pH (≈7) where V_{LG} was very small.

The solution pH was also measured in a constant current mode using PID control by setting α=33 (V_o=−1.5 V, d=300 nm). Figure 3d shows time-series measurements of phosphate buffered saline (PBS) solution at a bandwidth of 10 Hz. A switch was used to alternatively connect the ionic liquid-gate to the PBS solution and to ground. A histogram of the time-series was then used

to determine the uncertainty in the measurement and the pH resolution, δpH, as discussed further below. Figure 3e plots the change in V_{BG} with solution pH. Measurements were made relative to pH 7 (V_{LG}=0 V); acidic pH resulted in V_{LG}>0 V and basic pH in V_{LG}<0 V. A linear least-squares fit to the data returned a slope of 2.1 V/pH when α=33. Similar to measurements in Figure 2, sensitivity can be tuned by varying V_o to alter α. For example, when α=23 we obtained 1.2 V/pH, which could allow measurements over a larger range (*data not shown*). The maximum value of α obtained in the constant current mode was constrained by our control electronics, which can only source a maximum voltage of ±10V to control the back-gate voltage. This precluded measurements at the maximum value of α=159 for this device as seen from the static pH measurements in Figure 3c.

The pH resolution was also measured from the uncertainty in the time-series measurements (see *Methods* for a description) in Figure 3d. The mean uncertainty from the Figure, σ_{VBG} was found to be 300 μV. This value then resulted in δpH≈300×10^{-6} pH units (α=33), which was found to be consistent with the resolution obtained from noise measurements. Furthermore, since SNR, and thereby resolution, improves with increasing α as seen from Figure 2d, the best possible resolution of the device at the maximum gain (α=156) is predicted to be ≈70×10^{-6} pH units. This is consistent with the experimentally measured value of 92×10^{-6} pH units discussed above from an analysis of the noise floor (SNR 3; ≈10 dB) for a bandwidth of 10 Hz.[19]

Enzyme Activity and Kinetics. Protein kinases are an important subset of enzymes that facilitate post translational modifications, such as the phosphorylation of substrate proteins, to influence signaling pathways in the cell cycle and achieve homeostasis.[4,44] The deregulation of protein kinases is believed to underlie the onset of neurological conditions such as Alzheimer's disease or Parkinson's disease.[45,46] Therefore, the functional quantification of enzyme activity is

central to the development of therapeutics that restore physiological function.[47] Existing methods to measure enzyme activity, for example during protein phosphorylation, rely on radioactively labeled adenosine triphosphate (ATP) analogs or fluorophores. Such techniques are expensive because they need specialized molecule labeling and handling, require hours to yield results, and often alter the kinase activity, thus limiting their effectiveness in rapid therapeutic screening.[48,49]

We applied our ultra-sensitive FETs to measure the activity and kinetics of the proline-directed kinase Cdk5. Under normal physiological conditions, Cdk5 is tightly regulated by either the p35 or p39 inhibitory proteins.[7,50] Oxidative stress causes a 10 kDa membrane anchored fragment of p35 to be cleaved, forming the pathological activator p25, resulting in deregulation and delocalization of the complex to the cytosol.[51] The resulting pathological complex, Cdk5/p25, has higher activity than its physiological counterpart, Cdk5/p35, and participates in the indiscriminate phosphorylation of numerous proteins, which are known to result in neurofibrillary tangles that are a hallmark symptom of Alzheimer's disease.[52]

The multi-protein pathological complex, Cdk5/p25, participates in the phosphorylation reaction shown in Figure 4a. Cdk5 mediated phosphorylation results in the release of a proton during ATP hydrolysis and the transfer of a single phosphate group to either a serine or threonine residue immediately preceding a proline.[5] Here, we demonstrate the ability of ionic liquid-gated FETs to detect small changes in the solution pH during phosphorylation of the substrate protein, histone H1 (see *Methods* for reagent conditions).

Enzyme Activity. Figure 4b shows the change in $V_{t,BG}$ as a function of histone H1 concentration under steady-state conditions. In each case, $V_{t,BG}$ was obtained from an I_D-V_{BG} plot shown in Figure S6 (see *Supplementary Information*). To account for instrument drift, each data point in the figure was measured differentially with a control sample that was identical to the

measured vials except for the absence of ATP, thereby inhibiting the phosphorylation reaction. The kinase activity was then obtained using, $s = \gamma \frac{[H1]}{k + [H1]}$, where k is the activity coefficient, [H1] is the concentration of histone H1 and γ is a scaling constant. For the FET measurements in Figure 4b, we obtained k=17.5±1.3 μM from a non-linear regression of the model to the measured data, consistent with previously published activity measurements for the pathological Cdk5/p25 complex.[10] We compared the measurements in Figure 4b against enzyme activity measurements obtained from a radioactively labeled γ-^{32}P-ATP assay (see *Methods*) as seen in Figure 4c.[53] The value of k=12.1±2.3 μM from those measurements was found to be statistically consistent with the FET measurements with 95 % confidence.

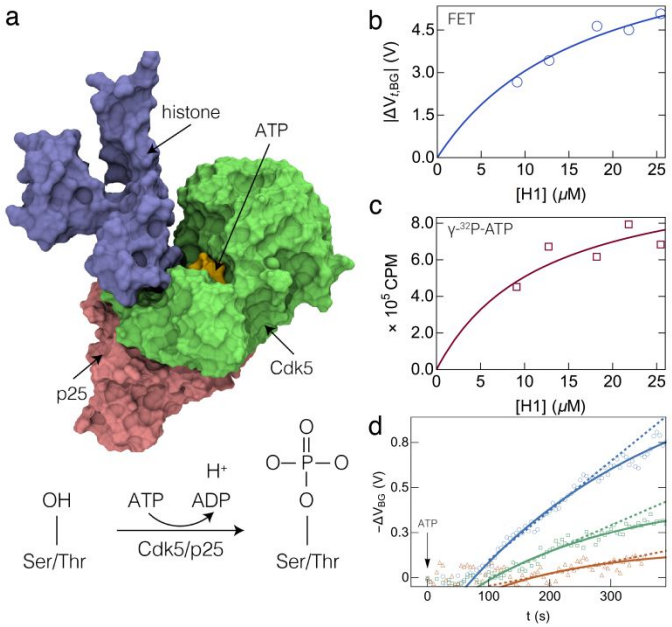

Figure 4: Ionic liquid-gate field-effect transistors (FET) were used for label-free enzyme activity and kinetics measurements. (a) The proline directed kinase Cdk5 catalyzes the phosphorylation of substrate proteins (e.g., histone H1) in the presence of an activator (e.g., p25) and adenosine triphosphate (ATP). The hydrolysis of ATP results in the transfer of a single phosphate group to either a serine (Ser) or threonine (Thr) residue in the substrate protein and the release of a proton into solution, resulting in a change in solution pH. (b) Ionic liquid-gate FETs (α=159) were used to measure the change in solution pH as a function of the histone H1 concentration ([H1]), and thereby infer the activity of Cdk5 under steady-state conditions. (c) The FET measurements were in quantitative agreement with a complementary assay that used radioactively labeled γ-^{32}P-ATP as a reporter of Cdk5 activity. (d) Time-series measurements of enzyme catalyzed phosphorylation as a function of [H1] (9.1 μM, △; 12.7 μM, □; 18.2 μM, ○) are shown and allow the direct estimation of the reaction dynamics. The solid lines depict the

reaction kinetics model that describes the time course of phosphorylation, while the dashed lines represent the reaction velocity during the first 100 s after a change in the signal was detected.

The change in the solution pH for the FET measurements was extracted from $\Delta V_{t,BG}$ in Figure 4b (α=159). The expected change in the solution pH was obtained using the expression $\frac{d[H^+]}{d\,pH} = -2.303\,\frac{C_a K_a [H^+]}{(K_a + [H^+])^2}$, where C_a is the buffer concentration, K_a is the acid dissociation constant and $[H^+]$ is the proton concentration.[11,54] The change in pH was consistent with ≈3 phosphorylation sites on the substrate protein, assuming an electrolyte solution buffered with C_a=250 μM 3-(*N*-morpholino)propanesulfonic acid (MOPS).

Enzyme Kinetics. The FET-based measurements have a response time that allows the direct estimation of reaction kinetics and velocities as seen from Figure 4d and Figure S6 (see *Supplementary Information*). The concentration of the Cdk5/p25 complex used in Figure 4d was 3.8 nM (5-fold lower than the quantity used in Figure 4b and c, and about 5-fold lower than the concentrations found in physiological conditions). A control sample without histone showed no change in the measured potential upon addition of ATP. From Figure 4d, we observed that upon addition of ATP there was a decrease in V_{BG} after ≈2 min. The polarity of V_{BG} is consistent with the release of protons into solution, which results in an increase in V_{LG}. The initial reaction velocities were extracted from a linear regression of the data for the first 100 s after a change in V_{BG} was detected and were found to increase monotonically with [H1]. Furthermore, the initial linear change in V_{BG} is consistent with an enzyme-limited reaction.[55] Finally, the time-course of each reaction in Figure 4d was fit with a first order rate law of the form, $V_{BG} = \beta(1 - e^{-k_1 t})$, where β is a scaling constant and k_1 is a rate constant. The rate constant was consistent with previously reported values[55,56] and found to be k_1=0.18±0.02 per min, independent of the histone

H1 concentration. FET-based measurements are in excellent quantitative agreement with existing techniques as seen from Figure 4, while providing results in minutes.

Based on the measurements in Figure 4 and the value of δpH determined experimentally from Figure 3, the ultimate limit of detection (LOD) for Cdk5/p25 can be substantially lower than the value of 3.8 nM demonstrated here. When tested under weak buffering conditions (Figure 4), the change in the pH measured for the lowest concentration of histone H1 (9.1 μM) was found to be 0.02 pH units at 300 s. Decreasing the concentration of Cdk5/p25 will require a longer time for the solution pH to reach a comparable value under an identical histone H1 concentration. However, the increased pH resolution of the ionic liquid gated FETs of 92×10^{-6} can allow the concentration of Cdk5/p25 to be decreased by 100-fold to 38 pM and still detect enzyme activity at 300 s. Under such conditions, we expect the change in pH to be $\approx200\times10^{-6}$, which is above the resolution of the sensors demonstrated in this work.

Conclusions

We have demonstrated that dual-gate FETs with atomically thin channels and ionic liquid top-gates allow performance limited by the intrinsic quantum capacitance of the channel material, providing a robust and sensitive biosensing platform. The nearly 100-fold improvement in pH sensitivity above the Nernst value and order of magnitude improvement in the resolution over state-of-the-art silicon ISFETs at a bandwidth of 10 Hz allowed the measurement of small changes in solution pH during enzyme mediated phosphorylation under physiological conditions. The method eliminates the need for specialized labeling and hazardous material handling and can decrease the cost and complexity of assays appreciably. Another key advantage of the measurements is that they are time-resolved, enabling the estimation of both enzyme activity and kinetics in a single assay. Because signal transduction is performed remotely, the measurements

are compatible with standard microtiter plates, and therefore amenable for use in high throughput screening to allow rapid evaluation of pharmaceutical candidates for neurological diseases.

The high sensitivity and SNR allowed measurements with 5-fold lower enzyme concentrations than physiological values and over an order of magnitude below previous demonstrations using FET. Furthermore, the pH resolution of 92×10^{-6} demonstrated in this study can result in a further improvement of the LOD of Cdk5/p25 to only 38 pM (or ≈500-fold lower than the physiological concentration). The vastly improved LOD can in turn enable new biomarker measurements in blood or cerebrospinal fluid to be developed for use at early stages of neurodegeneration where the changes to kinase activity are subtle and currently undetectable.[57,58] Importantly, these measurements can allow testing several years before any observable decline in cognitive function, allowing early interventions to be developed. The extended gate configuration of the sensors permit remote measurements, which allow them to be adapted for use in cell and tissue culture assays, where an increase in kinase activity has been correlated with pH imbalances.[59] Such measurements can allow assays that interrogate mechanistic behavior across multiple spatial scales – from test tube to cell culture experiments – to better quantify the origin of disease states.[60]

Conflicts of Interest

The authors declare no conflicts of interest.

Acknowledgements

S.T.L. acknowledges support by the National Institute of Standards and Technology (NIST) grant 70NANB16H170. J.B.K. and N.B.G. acknowledge support by NIST grant 70NAHB15H023. A.C. acknowledges support by the NIST grant 70NANB17H259. Research performed in part at the NIST Center for Nanoscale Science and Technology nanofabrication facility.

Footnotes

†Certain commercial equipment, instruments, or materials are identified in this paper in order to specify the experimental procedure adequately. Such identifications are not intended to imply recommendation or endorsement by the National Institute of Standards and Technology, nor it is intended to imply that the materials or equipment identified are necessarily the best available for the purpose.

References

1 K. S. Johnson, H. W. Jannasch, L. J. Coletti, V. A. Elrod, T. R. Martz, Y. Takeshita, R. J. Carlson and J. G. Connery, *Anal. Chem.*, 2016, **88**, 3249–3256.

2 C. Demuth, J. Varonier, V. Jossen, R. Eibl and D. Eibl, *Appl. Microbiol. Biotechnol.*, 2016, **100**, 3853–3863.

3 J. M. Rothberg, W. Hinz, T. M. Rearick, J. Schultz, W. Mileski, M. Davey, J. H. Leamon, K. Johnson, M. J. Milgrew, M. Edwards, J. Hoon, J. F. Simons, D. Marran, J. W. Myers, J. F. Davidson, A. Branting, J. R. Nobile, B. P. Puc, D. Light, T. A. Clark, M. Huber, J. T. Branciforte, I. B. Stoner, S. E. Cawley, M. Lyons, Y. Fu, N. Homer, M. Sedova, X. Miao, B. Reed, J. Sabina, E. Feierstein, M. Schorn, M. Alanjary, E. Dimalanta, D. Dressman, R. Kasinskas, T. Sokolsky, J. A. Fidanza, E. Namsaraev, K. J. McKernan, A. Williams, G. T. Roth and J. Bustillo, *Nature*, 2011, **475**, 348–352.

4 M. K. Tarrant and P. A. Cole, *Annu. Rev. Biochem.*, 2009, **78**, 797–825.

5 N. Bhalla, M. Di Lorenzo, G. Pula and P. Estrela, *Sci Rep*, 2015, **5**, 8687.

6 L. Mu, I. A. Droujinine, N. K. Rajan, S. D. Sawtelle and M. A. Reed, *Nano Lett.*, 2014, **14**, 5315–5322.

7 R. Dhavan and L. H. Tsai, *Nature Reviews Molecular Cell Biology*, 2001, **2**, 749–759.

8 G. Feldmann, A. Mishra, S.-M. Hong, S. Bisht, C. J. Strock, D. W. Ball, M. Goggins, A. Maitra and B. D. Nelkin, *Cancer Res*, 2010, **70**, 4460–4469.

9 A. Moutal, S. Luo, T. M. Largent-Milnes, T. W. Vanderah and R. Khanna, *Neurobiology of Pain*, 2018.

10 D. W. Peterson, D. M. Ando, D. A. Taketa, H. Zhou, F. W. Dahlquist and J. Lew, *P Natl Acad Sci USA*, 2010, **107**, 2884–2889.

11 D. D. Van Slyke, *Journal of Biological Chemistry*, 1922.

12 K. McLaughlin, A. Dickson, S. B. Weisberg, K. Coale, V. Elrod, C. Hunter, K. S. Johnson, S. Kram, R. Kudela, T. Martz, K. Negrey, U. Passow, F. Shaughnessy, J. E. Smith, D. Tadesse, L. Washburn and K. R. Weis, *Regional Studies in Marine Science*, 2017, **12**, 11–18.

13 R. P. Buck, S. Rondinini, F. G. K. Baucke, C. M. A. Brett, M. F. Camões, M. J. T. Milton, T. Mussini, R. Naumann, K. W. Pratt, P. Spitzer and G. S. Wilson, *Pure Appl. Chem.*, 2002, **74**, 2169–2200.

14 S. Loucaides, V. M. C. Rèrolle, S. Papadimitriou, H. Kennedy, M. C. Mowlem, A. G. Dickson, M. Gledhill and E. P. Achterberg, *Sci Rep*, 2017, **7**, 2481.

15 R. Gotor, P. Ashokkumar, M. Hecht, K. Keil and K. Rurack, *Anal. Chem.*, 2017, **89**, 8437–8444.

16 T. Wu, A. Alharbi, K.-D. You, K. Kisslinger, E. A. Stach and D. Shahrjerdi, *ACS Nano*, 2017, **11**, 7142–7147.

17 S. Zafar, C. D'Emic, A. Afzali, B. Fletcher, Y. Zhu and T. Ning, *Nanotechnology*, 2011, **22**, 405501.
18 A. Tarasov, D. W. Gray, M.-Y. Tsai, N. Shields, A. Montrose, N. Creedon, P. Lovera, A. O'Riordan, M. H. Mooney and E. M. Vogel, *Biosens Bioelectron*, 2016, **79**, 669–678.
19 E. Accastelli, P. Scarbolo, T. Ernst, P. Palestri, L. Selmi and C. Guiducci, *Biosensors (Basel)*, 2016, **6**.
20 R. Freeman, R. Gill and I. Willner, *Chem. Commun. (Camb.)*, 2007, 3450–3452.
21 N. Bhalla, M. Di Lorenzo, G. Pula and P. Estrela, *Biosens Bioelectron*, 2014, **54**, 109–114.
22 N. K. Rajan, K. Brower, X. Duan and M. A. Reed, *APPLIED PHYSICS LETTERS*, 2014, **104**, 084106.
23 W. U. Wang, C. Chen, K.-H. Lin, Y. Fang and C. M. Lieber, *P Natl Acad Sci USA*, 2005, **102**, 3208–3212.
24 K. Blennow, B. Dubois, A. M. Fagan, P. Lewczuk, M. J. de Leon and H. Hampel, *Alzheimers Dement*, 2015, **11**, 58–69.
25 F. Patolsky and C. Lieber, *Materials Today*, 2005, **8**, 20–28.
26 S. Zafar, M. Khater, V. Jain and T. Ning, *Appl. Phys. Lett.*, 2015, **106**, 063701–5.
27 X. Duan, Y. Li, N. K. Rajan, D. A. Routenberg, Y. Modis and M. A. Reed, *Nature Nanotech*, 2012, **7**, 1–7.
28 S. C. Su and L.-H. Tsai, *Annu. Rev. Cell Dev. Biol.*, 2011, **27**, 465–491.
29 N. B. Guros, S. T. Le, S. Zhang, B. A. Sperling, J. B. Klauda, C. A. Richter and A. Balijepalli, *ACS Appl. Mater. Interfaces*, 2019, **11**, 16683–16692.
30 S. B. Desai, S. R. Madhvapathy, M. Amani, D. Kiriya, M. Hettick, M. Tosun, Y. Zhou, M. Dubey, J. W. Ager III, D. Chrzan and A. Javey, *Adv. Mater.*, 2016, **28**, 4053–4058.
31 M. M. Perera, M.-W. Lin, H.-J. Chuang, B. P. Chamlagain, C. Wang, X. Tan, M. M.-C. Cheng, D. Tománek and Z. Zhou, *ACS Nano*, 2013, **7**, 4449–4458.
32 Y. J. Zhang, T. Oka, R. Suzuki, J. T. Ye and Y. Iwasa, *Science*, 2014, **344**, 725–728.
33 N. Ma and D. Jena, *2D Mater.*, 2015, **2**, 015003.
34 Y. Taur and T. H. Ning, *Fundamentals of Modern VLSI Devices*, Cambridge University Press, 2013.
35 L. Chu, H. Schmidt, J. Pu, S. Wang, B. Özyilmaz, T. Takenobu and G. Eda, *Sci Rep*, 2014, **4**, 7293.
36 A. Tarasov, W. Fu, O. Knopfmacher, J. Brunner, M. Calame and C. Schönenberger, *Appl. Phys. Lett.*, 2011, **98**, 012114.
37 B. Radisavljevic, A. Radenovic, J. Brivio, V. Giacometti and A. Kis, *Nature Nanotech*, 2011, **6**, 147–150.
38 J. Go, P. R. Nair and M. A. Alam, *Journal of Applied Physics*, 2012, **112**, 34516.
39 A. Ortiz-Conde, F. Sánchez, J. J. Liou and A. Cerdeira, *Microelectron. Reliab.*, 2002, **42**, 583–596.
40 H.-J. Jang and W.-J. Cho, *Sci Rep*, 2014, **4**, 5284.
41 R. Addou, S. McDonnell, D. Barrera, Z. Guo, A. Azcatl, J. Wang, H. Zhu, C. L. Hinkle, M. Quevedo-Lopez, H. N. Alshareef, L. Colombo, J. W. P. Hsu and R. M. Wallace, *ACS Nano*, 2015, **9**, 9124–9133.
42 Y. Yoon, K. Ganapathi and S. Salahuddin, *Nano Lett.*, 2011, **11**, 3768–3773.
43 A. V. Oppenheim and R. W. Schafer, *Discrete-Time Signal Processing*, Prentice Hall, 1999.
44 C. J. Sherr and J. M. Roberts, *Genes Dev.*, 2004, **18**, 2699–2711.
45 C. X. Gong and K. Iqbal, *Curr. Med. Chem.*, 2008, **15**, 2321–2328.

46 R. B. Maccioni, J. P. Muñoz and L. Barbeito, *Archives of Medical Research*, 2001, **32**, 367–381.
47 H. Ma, S. Deacon and K. Horiuchi, *Expert Opin Drug Discov*, 2008, **3**, 607–621.
48 Y. Wang and H. Ma, *Drug Discov Today Technol*, 2015, **18**, 1–8.
49 D. M. Goldstein, N. S. Gray and P. P. Zarrinkar, *Nat Rev Drug Discov*, 2008, **7**, 391–397.
50 N. D. Amin, W. Albers and H. C. Pant, *J. Neurosci. Res.*, 2002, **67**, 354–362.
51 M. S. Lee, Y. T. Kwon, M. Li, J. Peng, R. M. Friedlander and L. H. Tsai, *Nature*, 2000, **405**, 360–364.
52 W. Noble, V. Olm, K. Takata, E. Casey, O. Mary, J. Meyerson, K. Gaynor, J. LaFrancois, L. Wang, T. Kondo, P. Davies, M. Burns, Veeranna, R. Nixon, D. Dickson, Y. Matsuoka, M. Ahlijanian, L.-F. Lau and K. Duff, *Neuron*, 2003, **38**, 555–565.
53 B. K. Binukumar, Y.-L. Zheng, V. Shukla, N. D. Amin, P. Grant and H. C. Pant, *J. Alzheimers Dis.*, 2014, **39**, 899–909.
54 V. Chiriac and G. Balea, *J Chem Educ*, 1997, **74**, 937.
55 M. Liu, S. Choi, G. D. Cuny, K. Ding, B. C. Dobson, M. A. Glicksman, K. Auerbach and R. L. Stein, *Biochemistry*, 2008, **47**, 8367–8377.
56 M. Hashiguchi, T. Saito, S.-I. Hisanaga and T. Hashiguchi, *J. Biol. Chem.*, 2002, **277**, 44525–44530.
57 B. Dubois, H. H. Feldman, C. Jacova, H. Hampel, J. L. Molinuevo, K. Blennow, S. T. DeKosky, S. Gauthier, D. Selkoe, R. Bateman, S. Cappa, S. Crutch, S. Engelborghs, G. B. Frisoni, N. C. Fox, D. Galasko, M.-O. Habert, G. A. Jicha, A. Nordberg, F. Pasquier, G. Rabinovici, P. Robert, C. Rowe, S. Salloway, M. Sarazin, S. Epelbaum, L. C. de Souza, B. Vellas, P. J. Visser, L. Schneider, Y. Stern, P. Scheltens and J. L. Cummings, *Lancet Neurol*, 2014, **13**, 614–629.
58 G. B. Frisoni, M. Boccardi, F. Barkhof, K. Blennow, S. Cappa, K. Chiotis, J.-F. Démonet, V. Garibotto, P. Giannakopoulos, A. Gietl, O. Hansson, K. Herholz, C. R. Jack, F. Nobili, A. Nordberg, H. M. Snyder, M. Ten Kate, A. Varrone, E. Albanese, S. Becker, P. Bossuyt, M. C. Carrillo, C. Cerami, B. Dubois, V. Gallo, E. Giacobini, G. Gold, S. Hurst, A. Lönneborg, K.-O. Lovblad, N. Mattsson, J. L. Molinuevo, A. U. Monsch, U. Mosimann, A. Padovani, A. Picco, C. Porteri, O. Ratib, L. Saint-Aubert, C. Scerri, P. Scheltens, J. M. Schott, I. Sonni, S. Teipel, P. Vineis, P. J. Visser, Y. Yasui and B. Winblad, *Lancet Neurol*, 2017, **16**, 661–676.
59 C. A. Briggs, S. Chakroborty and G. E. Stutzmann, *Biochem. Biophys. Res. Commun.*, 2017, **483**, 988–997.
60 N. D. Amin, Y. Zheng, B. Bk, V. Shukla, S. Skuntz, P. Grant, J. Steiner, M. Bhaskar and H. C. Pant, *Molecular Biology of the Cell*, 2016, **27**, 3221–3232.

TOC Image

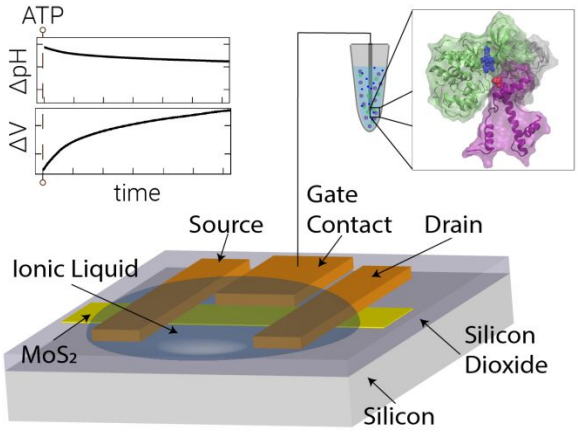

Atomically thin, quantum capacitance limited, field-effect transistors, enable measurements of biological enzymes implicated in Alzheimer's disease with unprecedented resolution.